



Contents lists available at ScienceDirect

# Journal of Materiomics

journal homepage: [www.journals.elsevier.com/journal-of-materiomics/](http://www.journals.elsevier.com/journal-of-materiomics/)

## Research paper

# Site preference of Ni in $\text{Pb}(\text{Fe}_{1/2}\text{Nb}_{1/2})\text{O}_3$ during additive compositional modification



Ahrom Ryu <sup>a, b, 1</sup>, Ji-Hun Park <sup>c, 1</sup>, Dong Won Jeon <sup>d, e</sup>, Jae-Hyeon Cho <sup>c</sup>, Haena Yim <sup>a</sup>, Keun Hwa Chae <sup>f</sup>, Seong H. Kim <sup>g</sup>, Sahn Nahm <sup>b</sup>, Sung Beom Cho <sup>d, e</sup>, Wook Jo <sup>c, \*\*</sup>, Ji-Won Choi <sup>a, h, \*</sup>

<sup>a</sup> Electronic Materials Research Center, Korea Institute of Science and Technology, Seoul, 02792, Republic of Korea

<sup>b</sup> Department of Material Science and Engineering, Korea University, Seoul, 02841, Republic of Korea

<sup>c</sup> Department of Materials Science and Engineering, Ulsan National Institute of Science and Technology (UNIST), Ulsan, 44919, Republic of Korea

<sup>d</sup> Department of Energy Systems Research, Ajou University, Suwon, 16499, Republic of Korea

<sup>e</sup> Department of Materials Science and Engineering, Ajou University, Suwon, 16499, Republic of Korea

<sup>f</sup> Advanced Analysis Center, Korea Institute of Science and Technology, Seoul, 02792, Republic of Korea

<sup>g</sup> Department of Chemical Engineering and Materials Research Institute, Pennsylvania State University, University Park, PA, 16802, USA

<sup>h</sup> Nanoscience and Technology, KIST School, University of Science and Technology, Seoul, 02792, Republic of Korea

## ARTICLE INFO

### Article history:

Received 8 April 2024

Received in revised form

28 May 2024

Accepted 6 June 2024

Available online 5 July 2024

## ABSTRACT

Doping and substitution methods are predominantly employed in the synthesis of ceramics to achieve their desired functional properties. We studied the behavior of excessive dopants in addition to an existing stoichiometric composition using a high-throughput continuous compositional spread sputtering method. We paid attention to the possible formation of thermodynamically unstable phases by the addition of an excessive amount of dopants. We showed that even when dopants were added as an additive, they dissolved into the existing lattice due to the benefit of the entropy of mixing. Regardless of excessiveness, all added elements incorporated into the lattice, stabilized by the tolerance factor. We also demonstrated our findings exemplarily with lead iron niobate to induce magnetic properties alongside inherent ferroelectricity ( $M_S = 10 \text{ emu/cm}^3$ ,  $P_S = 16 \mu\text{C}/\text{cm}^2$ ). We compare the results from CCS with those from the non-additive solid-state method, leading to a conclusion that the benefit from the entropy of mixing allows foreign elements to substitute for the elements initially residing in the lattice to a degree in compliance with the Goldschmidt tolerance factor. This observation was confirmed by a density functional theory calculation. We anticipate that our study could necessitate intensive research on achieving desired composition through industry-friendly processing.

© 2024 The Authors. Published by Elsevier B.V. on behalf of The Chinese Ceramic Society. This is an open access article under the CC BY license (<http://creativecommons.org/licenses/by/4.0/>).

## 1. Introduction

Electroceramics rely on their outstanding electrical properties to perform various functions in the fields of energy conversion and storage, communications, electronics, and automation, serving as essential components [1–9]. The functional properties of electroceramics are highly sensitive to its compositional variation typically

practiced by chemical doping [10–14]. Given that the dopants for electroceramics are mainly for defect engineering as donors or acceptors, they should, in principle, be substituted for the existing elements sitting at the intended lattice site. However, doping is commonly practiced by adding dopants as excess additives in industry and is well-known in semiconductor and multi-layer ceramic capacitor (MLCC) manufacturing. Especially, in the case of the MLCC industry, doping as additives is unavoidable, because they need to frequently change compositions in response to the market demand. Nevertheless, this so-called dopants-as-additives (DaA) strategy is obviously working. This is largely because the intended stoichiometry is, in fact, defective due to the limited purity level of starting powders. It is noted that the highest level of purity grade, i.e., ACS or reagent grade defines not less than 95 %. It

\* Corresponding author. Electronic Materials Research Center, Korea Institute of Science and Technology, Seoul, 02792, Republic of Korea.

\*\* Corresponding author.

E-mail addresses: [wookjo@unist.ac.kr](mailto:wookjo@unist.ac.kr) (W. Jo), [jwchoi@kist.re.kr](mailto:jwchoi@kist.re.kr) (J.-W. Choi).

Peer review under responsibility of The Chinese Ceramic Society.

<sup>1</sup> These authors equally contributed to this work.

is evident that the DaA method has been successfully utilized in the industrial field; however, there is a need to experimentally validate the gap between theoretical and practical implementations.

On the other hand, the phase stability of perovskite structured oxides ( $\text{ABO}_3$ ) is commonly estimated by the Goldschmidt tolerance factor which states that the phase stability is guaranteed when relatively large and smaller doping elements are substituted A and B cations, respectively [15–18]. This means that in the case of widely used Pb-based oxides, transition metals are only allowed to be substituted for B cations. However, it has been shown that even the relatively smaller ions, exemplarily Co and Ni, can be substituted for Pb ions in the A site to a certain degree without jeopardizing the phase stability during the conventional solid-state reaction method, by which even a compulsory substitution is possible [19–21]. This raises a concern that there is a chance that dopants applied through DaA go into unintended sites.

To address this issue, we made a systematic investigation on the site preference for the dopants as DaA using lead ion niobate (PFN,  $\text{Pb}(\text{Fe}_{1/2}\text{Nb}_{1/2})\text{O}_3$ )–NiO system as a model system. PFN is a multiferroic system, where ferroelectricity and antiferromagnetism coexist [22]. It is known that when Ni is substituted for Fe in the B site, PFN develops into a room-temperature multiferroic with ferromagnetism, more precisely ferrimagnetism [23]. Given that Ni as DaA can replace Pb in the A site, Fe in the B site, and Nb in the B site at the same time, PFN was chosen for this study in that the multiferroic property of PFN changes only when Ni replaces Fe in the B site. Therefore, PFN is a good system to check the site preference for Ni.

To realize a PFN–NiO system with a continuous compositional variation, we employed the so-called continuous composition spread (CCS) approach. The CCS sputtering process involves deposition using two targets mounted facing each other on sputtering guns. The substrate is positioned horizontally just below the device. The deposition rate decreases geometrically with the distance from the target; thus, supplying power simultaneously to both sputtering guns results in a natural diffusion of composition [24]. Through this method, various compositions can be obtained at incremental substitution levels. Therefore, it is conducive to gaining insights into new component designs or enhanced component performance. The CCS sputtering method provides a means to systematically explore a broad range of compositions through a single co-sputtering step; thereby, effectively screening binary or ternary composition spaces.

From the CCS, we achieved compositions with varying additive contents within a single thin film. We observed that Ni could dissolve into B site up to about 25% (in mole) and the substitution was specifically for Fe. It means that dopants as DaA prefer to replace ions of a similar size, which shares the same physical basis with the Goldschmidt tolerance factor. This result is also verified with the density functional theory (DFT) calculations. Consequently, our experiment is significant in that it experimentally demonstrates that the DaA method can produce doping-like effects in materials without precise site control. Also, our result implies that given that the compositions reported to have specific functionality in literature are commonly achieved by stoichiometric compositional modification, one should take additional measure to compensate the unavoidable entropy contribution to obtain a desired composition during mass production through additive compositional modification.

## 2. Experimental section

The PFN–NiO thin films were prepared by co-sputtering pristine PFN and NiO targets located at 90° off-axis from the sputtering gun, i.e., the continuous composition spread (CCS) sputtering method. We prepared pristine PFN and NiO targets using the solid-state reaction method, by referring to previous studies [25]. The PFN–NiO thin films were deposited on Si substrates with dimensions of 75 mm × 5 mm, after cleaning the substrate using sonication with acetone, ethanol, and deionized water. The deposition was carried out at 1.99 Pa and room temperature in a chamber filled with Ar atmosphere; the flow rate of gas was controlled by a mass flow controller. The sputtering power densities for PFN and NiO targets were 4.9 W/cm<sup>2</sup> and 1.5 W/cm<sup>2</sup>, respectively. The radio frequency (RF) power was determined by considering pre-experimental data, where the thin film was deposited with variable RF power using each target (Fig. S1 and Fig. S2). We heat-treated PFN–NiO thin films at 700 °C for 2 h and cut down them into 15 pieces of 5 mm × 5 mm size to differentiate the Ni content. The obtained thin film pieces were patterned into various sizes of dot arrays using the photolithography method and then coated with 70 nm of thickness Pt deposited by DC sputtering at room temperature as a top electrode for measuring electric properties. Each specimen was labeled as Px ( $x = 1, 2, \dots, 15$ ) based on its position; for example, the specimen closest to the PFN target was labeled as P01. The cross-sectional microstructure of thin films was prepared to determine their thickness and quality using scanning electron microscopy (FE-SEM, Inspect 50, FEI, USA) along with elementary information performed by energy-dispersive spectrometry (EDS). X-ray diffraction (XRD) patterns were obtained using an X-ray diffractometer (DMAX 2200, Rigaku, Tokyo, Japan) with Cu K $\alpha$  radiation ( $\lambda = 1.54 \text{ \AA}$ ) with a voltage of 40 kV and a current of 200 mA at a scanning rate of 2 (°)/min in the 2 $\theta$  range from 15° to 80°. High-resolution transmittance electron microscopy (HRTEM) analysis were employed to obtain structural information of thin films. XAS and EXAFS were used to determine the interatomic distance and position of Ni and Fe (PAL-XFEL). X-ray photoelectron spectroscope (XPS) analysis was implemented to analyze the oxidation state and binding state of Ni and Fe ions (K-alpha, ThermoFisher). The dielectric properties, i.e., relative permittivity and dielectric loss, were evaluated at room temperature using an impedance analyzer (E4990A, Agilent Technologies, USA). The ferroelectric measurement system (Precision Premier II, Radian Technology, USA) was used to measure the ferroelectric hysteresis loops at room temperature. Room-temperature magnetic hysteresis loops were measured using a vibrating sample magnetometer (EZ9 VSM, MicroSense, USA).

All the density functional theory (DFT) calculations were conducted using the Vienna ab-initio simulation package (VASP) [26]. These calculations employed the projector-augmented wave (PAW) method [27], with the exchange-correlation potential described by the generalized gradient approximation (GGA) within the Perdew-Burke-Ernzerhof (PBE) parameterization [28]. Computational parameters included plane-wave cut-off energy of 520 eV and k-point meshes  $2 \times 2 \times 1$  for Brillouin zone sampling, determined through convergence tests. Special quasi-random structures (SQS) for the alloy systems were generated using an 80-atom supercell with the mcsqs code from the Alloy Theoretic Automated Toolkit [29]. The Gibbs free energy of mixing was computed to determine the site preference of the Ni via PFN substitution. This is expressed as:

$$\Delta G_{\text{mix}}(x, T) = \Delta H_{\text{mix}}(x) - T \bullet \Delta S_{\text{mix}}(x)$$

where  $x$  represents the atomic fraction of Ni,  $T$  denotes the temperature, and  $\Delta H_{\text{mix}}$  and  $\Delta S_{\text{mix}}$  refer to the mixing enthalpy and entropy, respectively. The entropy of mixing  $\Delta S_{\text{mix}}(x)$  is defined as:

$$\Delta S_{\text{mix}}(x) = -nk_B[x \ln(x) + (1-x)\ln(1-x)]$$

where  $k_B$  is the Boltzmann constant with a value of  $8.8617 \times 10^{-5}$  eV/K, and  $n$  represents the degeneracy of the cation sites. The enthalpy of mixing  $\Delta H_{\text{mix}}$  is calculated as:

$$\Delta H_{\text{mix}} = H_{\text{alloy}} - \sum_i x_i H_i$$

where  $H_{\text{alloy}}$  represents the total energy of the Ni-doped PFN structure representing the random alloy, and  $x_i$  and  $H_i$  denote the fractional and total energies of the possible precursor of the Ni-doped PFN, such as PbO, Fe<sub>2</sub>O<sub>3</sub>, Nb<sub>2</sub>O<sub>5</sub>, and NiO, respectively.

### 3. Results and discussion

#### 3.1. Sample preparation

**Fig. 1a** presents a schematic illustration of the continuous composition spread (CCS) sputtering method with PFN and NiO targets. The different applied RF power to each target, *i.e.*, 100 W and 30 W for PFN and NiO targets, respectively, was determined to meet our strategy, *i.e.*, inducing multiferroicity in PFN-based compositions by introducing Ni ions. The cross-sectional microstructure images of PFN-NiO thin films (**Fig. 1c**), which were cut into 15 equal-sized pieces for comparison depending on the compositions, demonstrate that all compositions were well-deposited on the substrate using the CCS method. It was estimated that the thickness of thin film gradually decreases from 900 nm to 400 nm as it is deposited away from the PFN target, before becoming saturated at 400 nm after P12 composition, as indicated in **Fig. 1b**. The thickness of each deposited film was plotted in comparison with the thickness of separately deposited PFN and NiO (**Fig. 1b**) and their sum. As expected, the thickness of co-sputtered PFN-NiO thin films is smaller than the sum of the separately deposited PFN and NiO films,

which implies that a certain degree of NiO dissolved into the PFN lattice. The unique feature of CCS is well-reflected in the gradual increase and decrease in Pb and Ni content, evidenced by an energy-dispersive spectrometry (EDS) analysis as a function of the distance from the PFN target as shown in **Table S1**.

#### 3.2. X-ray diffraction & transmission electron microscopy

**Fig. 2a** displays the phase evolution during the co-sputtering of PFN and NiO. The XRD pattern revealed that  $x = 1$  to  $x = 4$  exhibits a single-phase perovskite structure within the resolution limit of the apparatus employed, while the blocks of  $x > 4$  contain non-perovskite phases, *i.e.* pyrochlore ( $\text{Pb}_3\text{Nb}_4\text{O}_{13}$ , JCPDS No. 00-023-0352),  $\text{NiFe}_2\text{O}_4$  (JCPDS No. 01-086-2267), and NiO (JCPDS No. 00-047-1049) phases. The fact that the composition blocks show a complete solid solution between PFN and NiO up to  $\sim$  block #4 indicates that there is a solubility limit of NiO in PFN when they are co-sputtered. In the block #5, a pyrochlore phase started to appear and PFN structure was totally disintegrated on the block #8. Further, an increase in the distance from the PFN target induced a spinel-structured  $\text{NiFe}_2\text{O}_4$ , and finally unreacted NiO. It indicates that Ni ions were successfully introduced into the PFN system up to  $x = 5$  composition. Furthermore, the co-sputtered thin film has a thickness between that of the pristine PFN and the combined thickness of the pristine PFN and NiO, as shown in **Fig. 1**. These XRD and thickness data suggest that Ni has occupied one of the perovskite sites within the PFN up to  $x = 5$ . Additionally, Rietveld analysis for the P01 composition has been conducted as shown in **Fig. S3**. The lattice constant of the compositions increased slightly from P01 to P04 (from  $4.001 \text{ \AA}$  to  $4.007 \text{ \AA}$ ) and remained consistent up to the composition where the PFN structure is maintained (see **Fig. 2b**). This expansion in the lattice constant was due to the substitutional behavior of  $\text{Ni}^{2+}$  for  $\text{Fe}^{3+}$ , as the ionic radius of  $\text{Ni}^{2+}$  ( $0.69 \text{ \AA}$ ) is larger than that of  $\text{Fe}^{3+}$  ( $0.645 \text{ \AA}$ ), considering both oxidation state and coordination number. To investigate the crystal information of P04 composition further, high-resolution transmittance electron microscopy (HRTEM) was prepared; we chose the P04 specimen because it contains the most Ni ions without secondary phases (see **Fig. 2c**). It was observed in a high-angle annular dark field (HAADF) image that Pb and Fe/Nb ions are sitting at the A and B sites, respectively, which is consistent with the general perovskite

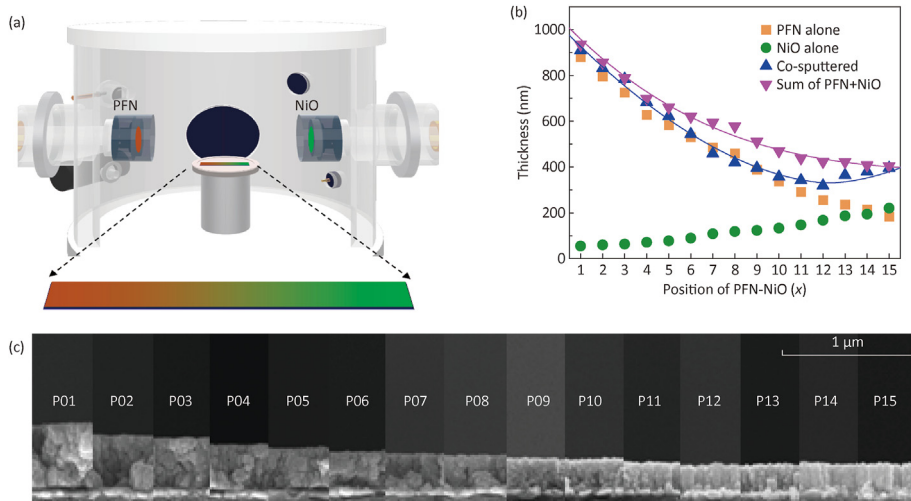


**Fig. 1.** Microstructure of PFN-NiO thin films prepared by continuous composition spread (CCS) sputtering method. (a) Schematic illustration of CCS method using PFN and NiO targets and (b) the estimated thickness of each thin film. (c) Cross-sectional microstructure images obtained by using scanning electron microscopy (SEM).

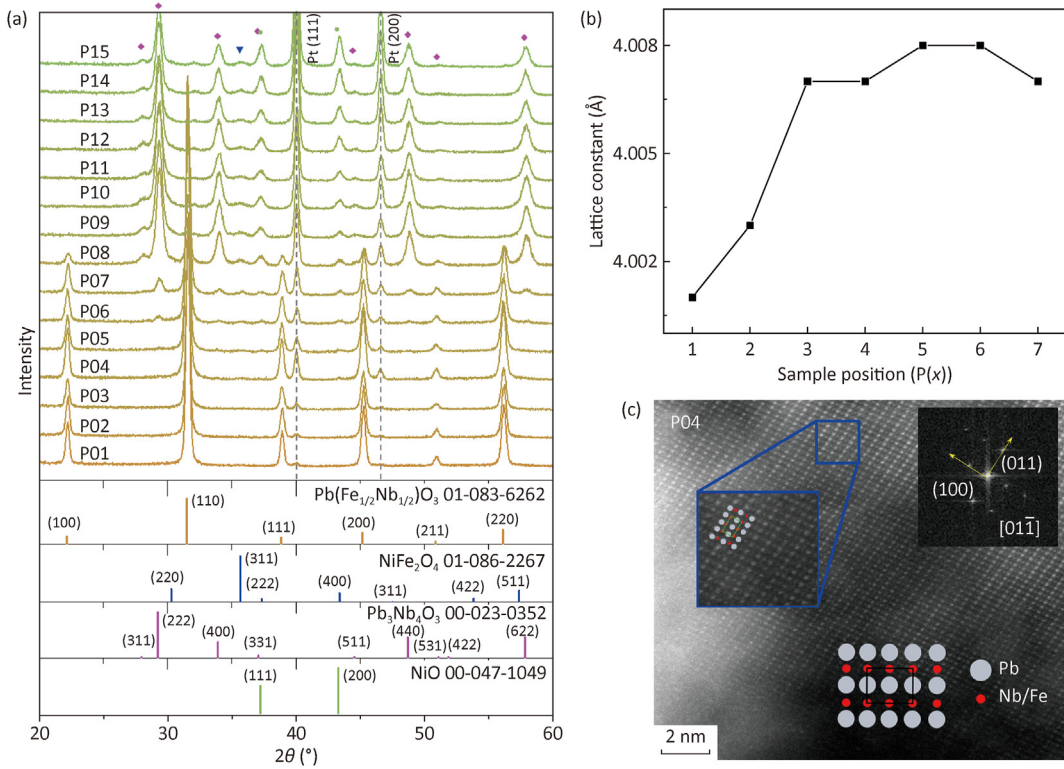


**Fig. 2.** Structural analysis of  $P(x)$  ( $x = 1, 2, 3, \dots, 15$ ) thin films. (a) X-ray diffraction (XRD) patterns of each composition block, and (b) lattice constant from P01 to P07. Exemplary high-resolution transmittance electron microscopy (HRTEM) images of P04 composition is shown on (c), chosen based on single-phase composition with the maximum Ni ions.

structure exhibiting the  $R\bar{3}c$  space group. The Fast Fourier Transform (FFT) image, which was obtained by converting the HRTEM image reveals that the crystal structure is well-indexed to the (100) and (011) diffraction with  $[0, \bar{1}, 1]$  of the zone-axis.

### 3.3. X-ray photoelectron spectroscopy & extended X-ray absorption fine structure

**Fig. 3** investigated XPS and XAS analysis on P04 thin film for Fe and Ni ions to analyze the oxidation states of both atoms and infer

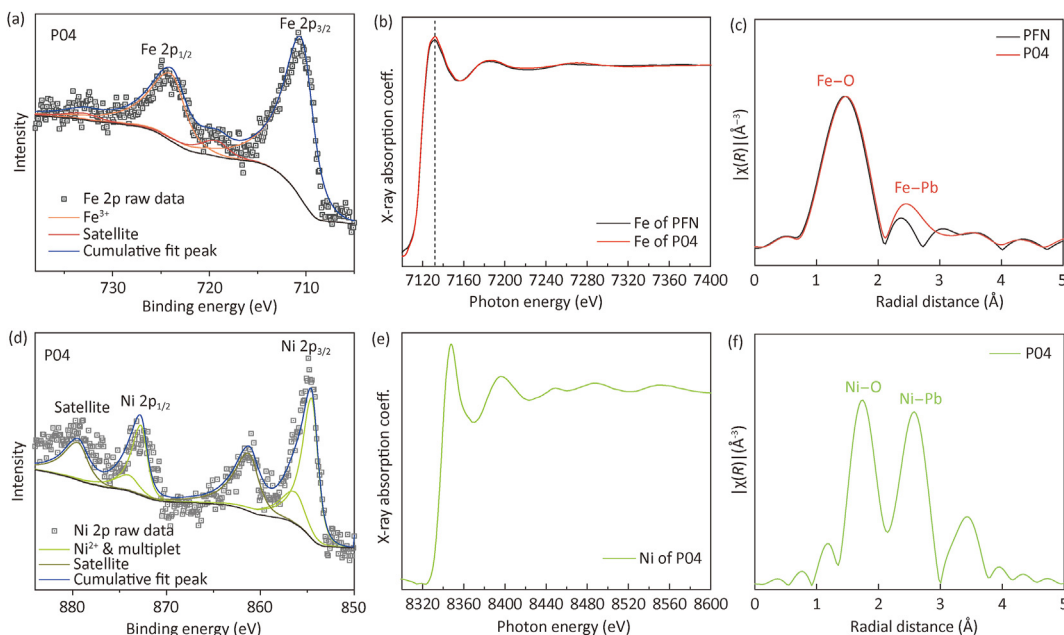


**Fig. 3.** X-ray photoelectron spectroscopy (XPS) and X-ray absorption spectroscopy (XAS) of P04 composition measured at room temperature. (a) XPS, (b) X-ray absorption near edge structure (XANES), and (c) extended X-ray absorption fine structure (EXAFS) profiles for Fe ion. (d–f) The same dataset for Ni ion.

the bonding state and atomic structure. We investigated XPS and XAS analysis on P04 thin film for spectating atomic structure with ionic radius and oxidation state for Fe and Ni ions [30–32].  $\text{Fe}^{3+}$  are spectated by XPS and it show the same tendency with pure PFN (Fig. S4, Fig. 3a). The Fe 2p peaks of PFN could be fitted with the  $2p_{3/2}$  and  $2p_{1/2}$  species and their satellites of one single component. The Fe 2p peaks of P04 (Fig. 3a) could be fitted with the same peaks with the same peak positions and shapes. If  $\text{Fe}^{2+}$  is formed, we expect the leading edge of the  $2p_{3/2}$  peak would have been significantly shifted to the lower BE side; but that is not seen in the data. So, the Fe oxidation state is not strongly affected by a small amount of nickel doping and remains close to 3+ [33] and it indicates that, despite the introduction of Ni, the pseudocubic perovskite structure similar to PFN was maintained. The Ni 2p peaks of P04 (Fig. 3d) could also be fitted with the  $2p_{3/2}$  and  $2p_{1/2}$  species and their satellites and multiplets of one single component using the same peak shape used for the Fe 2p peak fitting. Note that the secondary components in the high BE tail side of the Ni 2p<sub>3/2</sub> originates from the final state effects during the photoemission process, which is ubiquitously observed in XPS spectra of transition metal elements [34,35]. So, from the Ni 2p XPS analysis alone, it is difficult to determine the presence of the  $\text{Ni}^{3+}$  state and its abundance [36]. It shows that it is plausible that Ni ions were introduced into PFN system in  $\text{Ni}^{2+}$  form majorly. Given that XANES spectrum and Fe K-edge of Fe ions (Fig. 3b), the main peak of P04 shows almost the same energy level with pristine PFN (7132 eV). EXAFS data (Fig. 3c) indicates that the interatomic distance of Fe of P04 and neighbor ions are 1.50 Å with O (Fe–O), and 2.42 Å with Pb (Fe–Pb), respectively. Fe–Pb bonding distance is larger than that of pristine PFN (Fe–Pb for 2.36 Å). It implies that the bonding distance of Fe–Pb increased locally with remaining the average lattice constant steadily. The interatomic distance between Ni ions and their neighboring ions are 1.71 Å and 2.57 Å for Ni–O and Ni–Pb, respectively, which are little larger than that of Fe ions (Fig. 3f). The difference may be attributed to the introduction of Ni instead of Fe during co-sputtering, which appears to have induced this variation by causing minor lattice distortion and disrupting the Fe–O and Fe–Pb bonding at that site. Through X-ray analysis, it has been confirmed that a pseudocubic perovskite phase, which structurally resembles pure PFN, is maintained in P04. Also, XRD measurement data with the Goldschmidt tolerance factor suggests that the incorporation of Ni into the B-site is plausible. Additionally, the increased leakage current observed in the P04 sample during the subsequent ferroelectric hysteresis loop, compared to the pristine PFN (Fig. S4), suggests that cation vacancy defects were induced by the acceptor doping of  $\text{Ni}^{2+}$  replacing  $\text{Fe}^{3+}$ .

### 3.4. Density functional theory calculations

To investigate the site preference of Ni substitution within PFN, we conducted DFT calculations for the  $\text{Pb}_a\text{Fe}_b\text{Nb}_c\text{Ni}_d\text{O}_3$  alloy system. The detailed calculation method is outlined in the Experimental Details section. The alloying behavior and site preference of PFN + NiO were assessed using special quasi-random structures [29] to simulate the random occupation of  $\text{Fe}^{3+}$ ,  $\text{Nb}^{5+}$ , and  $\text{Ni}^{x+}$  at the B site of the PFN, as illustrated in Fig. 4a. By employing the regular solution model [37], we determined the enthalpy of mixing as a function of the atomic concentration of Ni in the  $\text{Pb}_a\text{Fe}_b\text{Nb}_c\text{Ni}_d\text{O}_3$  alloys. In this study, NiO was doped with the  $\text{Pb}(\text{Fe}_{0.5}\text{Nb}_{0.5})\text{O}_3$  and formed  $\text{Pb}_a\text{Fe}_b\text{Nb}_c\text{Ni}_d\text{O}_3$  ( $a + b + c + d = 2$ ). The enthalpy of the mixing ( $\Delta H_{\text{mix}}$ ) can be expressed as:

$$\Delta H_{\text{mix}} = E_{\text{Pb}_a\text{Fe}_b\text{Nb}_c\text{Ni}_d\text{O}_3}^{\text{DFT}} - aE_{\text{PbO}}^{\text{DFT}} - \frac{1}{2}bE_{\text{Fe}_2\text{O}_3}^{\text{DFT}} - \frac{1}{2}cE_{\text{Nb}_2\text{O}_5}^{\text{DFT}} - E_{\text{NiO}}^{\text{DFT}} - e\mu_0$$

To satisfy the stoichiometry, an additional oxygen atom was considered ( $\mu_0$ ), adhering to the relationship  $e = 3 - (a + \frac{3}{2}b + \frac{5}{2}c + d)$ . As depicted in Fig. 4b, Ni substitution at the Fe site appears to be more thermodynamically stable across the entire region compared to the Nb site. To determine the substitutable Ni concentration during heat treatment, we also computed the Gibbs-free energy of mixing at various temperatures. The Gibbs-free energy of mixing at 700 °C is negative for Ni substitution at the Fe site up to a concentration of about approximately 30% (in mole). This finding aligns with experimental observations indicating that Ni can dissolve into the B site at 25%, replacing  $\text{Fe}^{3+}$ .

### 3.5. Ferroelectric and ferromagnetic properties

Fig. 5 demonstrates the dielectric, ferroelectric, and ferromagnetic properties of deposited films. Interestingly, room-temperature multiferroicity, including dielectric, ferroelectric, and ferromagnetic properties, was demonstrated in PFN-NiO thin film systems that exhibit a single-phase perovskite with no secondary phases, i.e., pristine PFN ( $x = 0$ ) and P01, P02, P03, and P04 as shown in Fig. 5. P05 also has shown its multiferroic properties despite its secondary phases, but its decrease of ferroelectricity appeared. There are two considerable decreases in composition-dependent dielectric constant ( $\epsilon_r$ ), while all compositions exhibit prominent dielectric loss ( $\tan \delta$ ) less than 0.1; a sharp decrease between pristine PFN and P01, and between P06 and P07. Also, the consistent tendency is spectated on a ferroelectric hysteresis loop with a dielectric constant.

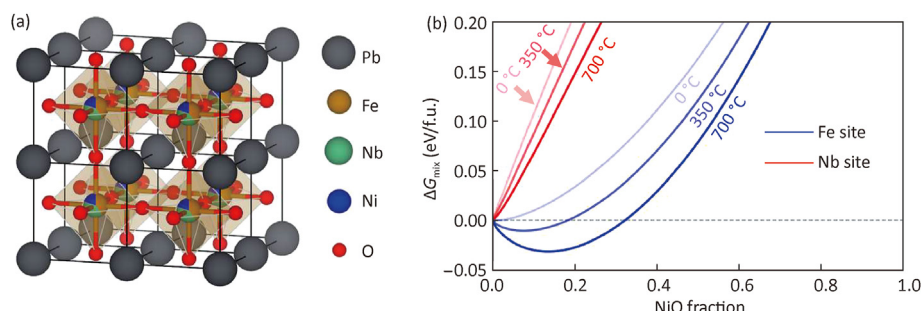


**Fig. 4.** (a) Atomic structure of the  $\text{Pb}_a\text{Fe}_b\text{Nb}_c\text{Ni}_d\text{O}_3$  alloy systems, where grey, brown, green, blue, and red atoms denote Pb, Fe, Nb, Ni, and O, respectively. (b) The effect of temperature on the Gibbs-free energy of mixing of  $\text{Pb}_a\text{Fe}_b\text{Nb}_c\text{Ni}_d\text{O}_3$  alloy systems at 0, 350 °C, and 700 °C. The blue line denotes Ni substitution at the Fe site, while the red line represents the Ni substitution at the Nb site.

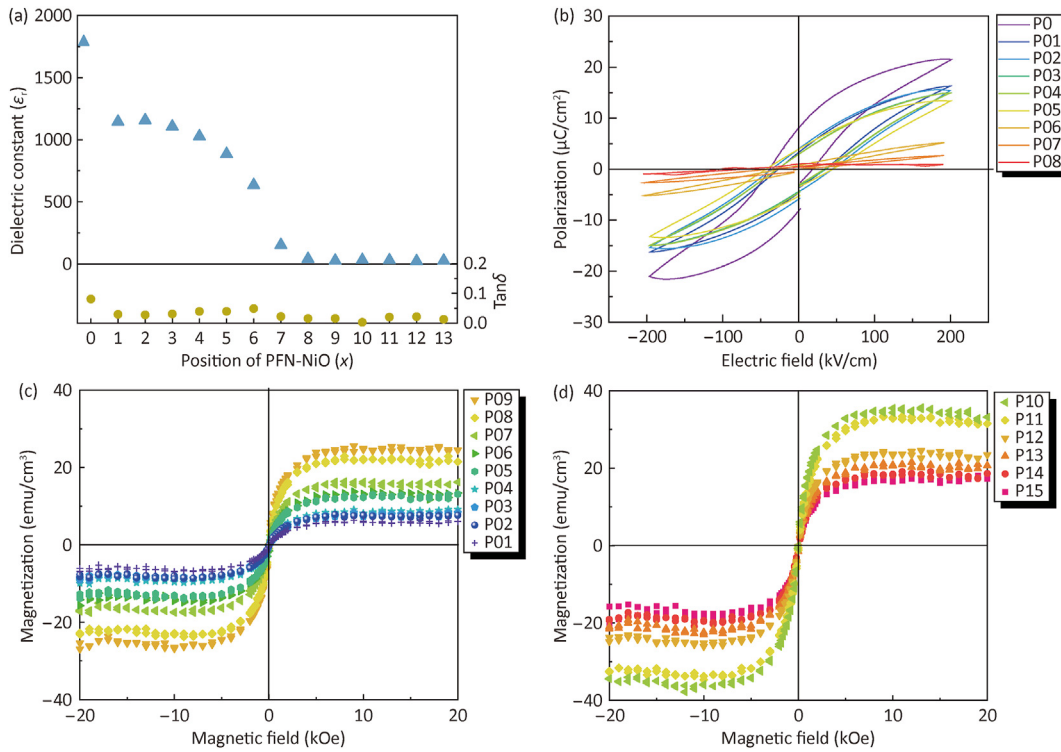


**Fig. 5.** Room-temperature multiferroicity of pristine PFN ( $x = 0$ ) and P( $x$ ) thin films. (a) Dielectric constant and loss with a measurement frequency at 100 Hz. (b) Ferroelectric hysteresis loops measured by applying an electric field of 200 kV/cm at 25 Hz for  $x = 0$  to  $x = 8$ . Magnetic hysteresis loops and their magnification with an application of a magnetic field of 20 kOe for (c)  $x = 1$ –9 and (d)  $x = 10$ –15.

The dielectric constant was not measured in P14 and P15, which gradually reaches from decreasing dielectric constant to limitation. It is considered that P14 and P15 samples have properties closer to pure NiO. P01 to P05 show a similar ferroelectric hysteresis loop with B-site substituted PFN and it continuously deteriorated when Ni was introduced. The saturation polarization, remanent polarization, and coercive field values of Ni-introduced PFN compositions were practically the same at  $\sim 16 \mu\text{C}/\text{cm}^2$ ,  $\sim 4 \mu\text{C}/\text{cm}^2$ , and  $\sim 36 \text{kV}/\text{cm}$ , respectively. It is reasonable that the gradual decrease in dielectric constant along with the increase in dielectric loss resulted from the formation of Fe-site engineered PFN [25]. After P05, the ferroelectric property is totally degraded as a conductor. From P09, we could not obtain significant ferroelectric data because the closer the position of the sample in the CCS sputter, the NiFe<sub>2</sub>O<sub>4</sub> spinel and pyrochlore secondary phase is dominant on compositions and it results in complete loss of dielectric and ferroelectric properties. It can be also evidenced by increasing spinel and pyrochlore peaks on XRD patterns. For CCS sputtered compositions, ferromagnetic hysteresis loops were observed at room temperature. Considering pristine PFN makes a paramagnetic hysteresis loop and Ni-introduced PFN makes a ferromagnetic hysteresis loop at room temperature [25], the graph from P01 to P15 can be explained in three parts.

P01–P05; Magnetization is increased while Ni is increased and it seems to be caused by the substitution of Ni in the Fe sites, resulting in increased net magnetization. There is no secondary phase on P01–P04 compositions and even a smidgen of secondary phase exists on the P05 composition, the trade-off relation of ferromagnetic and ferroelectric properties appears.

P06–P09; Magnetization also increased while Ni is increased. However, since the secondary phase is increased and the dielectric constant decreases rapidly, it seems to be a phenomenon caused by the formation of the NiFe<sub>2</sub>O<sub>4</sub> spinel composition beyond the Ni-substituted threshold.

P10–P15; Magnetization is generally higher in these compositions than in others, but this value is not proportional to the Ni ratio. In these compositions, the NiO ratio dominates, and NiFe<sub>2</sub>O<sub>4</sub> contributes significantly to magnetization. However, an unexpected amount of pyrochlore and NiO phase (antiferromagnetism) has an impact on magnetization.

After conducting structural analysis, we observed that P01 to P05 compositions exhibited similar properties when replacing Ni with a B-site element of PFN, in terms of both ferromagnetic and ferroelectric properties. Generally, substituting base materials in sputtering requires separate targets for each different composition. However, it has been demonstrated that the same outcomes as substitution can be induced by additives with the CCS sputtering method. Given that compositional substitution is very sensitive in multiferroic materials due to the trade-off relationship between ferroelectricity and ferromagnetism, the CCS sputtering method has many advantages in producing thin films. One notable point is that the blocks that appeared as a single phase entered only the B-site among the possible positions within the perovskite structure, which includes the A-site and B-site. This is considered to be influenced by the Goldschmidt tolerance factor, which serves as an indicator of stability and distortion within the crystal structure. According to the calculation formula ( $t = [r_A + r_X]/\sqrt{2[r_B + r_X]}$ , where  $r_A$ ,  $r_B$ ,  $r_X$  are ionic radii for ions in A, B, and X sites) [38], the

material shows cubic perovskite when  $0.9 < t < 1.0$ . Considering a pseudocubic phase observed in the XRD pattern of the pure PFN, the structure substituting Ni for Fe maintains a more stable structure since the ionic radii of  $\text{Ni}^{2+}$  (0.69 Å) is closer to those of  $\text{Fe}^{3+}$  (0.645 Å) than to that of  $\text{Pb}^{2+}$  (1.42 Å) for the tolerance factor ( $t_{\text{Fe} \rightarrow \text{Ni}} = 1.00$ ,  $t_{\text{Pb} \rightarrow \text{Ni}} = 0.72$ ). Here, what should be noted is that the ionic size of  $\text{Nb}^{5+}$  (0.64 Å) is not quite different from  $\text{Fe}^{3+}$ . It means that the tolerance factor is not the only criterion for phase stability. Although the excessively added  $\text{Ni}^{2+}$  evidently replaced  $\text{Fe}^{3+}$ , the typically reported internal bias field was not observed as consistent with our earlier study [25]. The current result strongly supports that in addition to the tolerance factor, a minimalization of charge difference also matters.

#### 4. Conclusions

We compared the behavior of materials with excessively added dopants to a stoichiometric composition. We employed the CCS sputtering method to distinctly confirm characteristic changes linked to compositional variations with a reference to multiferroic materials. We compared these results with previous research that involved doping some intended elements to specific sites within the same base material. We noted that the excessively added dopants tend to go into the lattice possibly due to the benefit from the increase in the entropy of mixing. As exemplarily demonstrated in Ni-doped PFN, a multiferroic property ( $M_S = 10 \text{ emu/cm}^3$ ,  $P_S = 16 \mu\text{C}/\text{cm}^2$ ) was induced at room temperature when up to 25% (in mole) of Ni ions were dissolved into the B-site, which is expected when Ni replaces Fe ions in the B-site. It means that the additionally added dopants have a clear preference on the site occupancy. In fact, Ni can replace all of the cations in  $\text{ABO}_3$  when it is intended to replace a specific target element, but this additionally added nickel replaces only iron possibly due to the ionic size and charge balance confinement. During the process of excess doping where atoms are deposited in ionic form, these results suggest that the atoms involved have sufficient energy to replace thermodynamically stable position firstly in reference to the Goldschmidt tolerance factor. Among the choices in the same lattice position, the minimalization of charge imbalance plays the most critical role. We anticipate that our research will serve as a foundation for studying how to design the desired composition through industry-friendly processes.

#### CRediT authorship contribution statement

**Ahrom Ryu:** Writing – original draft, Investigation. **Ji-Hun Park:** Writing – original draft, Formal analysis. **Dong Won Jeon:** Methodology, Data curation. **Jae-Hyeon Cho:** Writing – review & editing, Formal analysis. **Haena Yim:** Writing – review & editing. **Keun Hwa Chae:** Investigation, Data curation. **Seong H. Kim:** Data curation. **Sahn Nahm:** Supervision. **Sung Beom Cho:** Data curation. **Wook Jo:** Writing – review & editing, Supervision, Conceptualization. **Ji-Won Choi:** Writing – review & editing, Supervision, Conceptualization.

#### Declaration of interests

The authors declare that they have no known competing financial interests or personal relationships that could have appeared to influence the work reported in this paper.

#### Acknowledgments

This work was supported by the National Research Foundation of Korea (NRF) funded by the Ministry of Science and ICT(2021-M1A3B2A01078712). This research was supported by the Korea Institute of Science and Technology Future Resource Program (2E33181) & the National Research Foundation of Korea (NRF) grant by the Korea government (No.2021R1A2C2010695 & RS-2023-00222719).

#### Appendix A. Supplementary data

Supplementary data to this article can be found online at <https://doi.org/10.1016/j.jmat.2024.06.004>.

#### References

- [1] Spaldin NA, Ramesh R. Advances in magnetoelectric multiferroics. *Nat Mater* 2019;18:203–12.
- [2] Cho J-H, Jo W. A brief review on magnetoelectric multiferroic oxides. *J Korean Inst Electr Electron Mater Eng* 2021;34:149–66.
- [3] Fiebig M, Lottermoser T, Meier D, Trassin M. The evolution of multiferroics. *Nat Rev Mater* 2016;1:1–14.
- [4] Spaldin NA. Multiferroics beyond electric-field control of magnetism. *Proc R Soc A* 2020;476:20190542.
- [5] Hur N, Park S, Sharma PA, Ahn J, Guha S, Cheong S-W. Electric polarization reversal and memory in a multiferroic material induced by magnetic fields. *Nature* 2004;429:392–5.
- [6] Lee JH, Yeo TS, Jo W. Enhanced dielectric reliability in the X9R-type  $\text{Bi}_{1/2}\text{Na}_{1/2}\text{TiO}_3\text{-CaZrO}_3$  relaxor ferroelectric ceramics. *J Am Ceram Soc* 2024;107:4252–62.
- [7] Hu J-M, Nan C-W. Opportunities and challenges for magnetoelectric devices. *Apl Mater* 2019;7:080905.
- [8] Jo W, Dittmer R, Acosta M, Zang J, Groh C, Sapper E, et al. Giant electric-field-induced strains in lead-free ceramics for actuator applications—status and perspective. *J Electroceram* 2012;29:71–93.
- [9] Zate TT, Ko N-R, Yu H-L, Choi W-J, Sun J-W, Jeon J-H, et al. Textured ceramics for Multilayered actuator applications: challenges, trends, and perspectives. *J Korean Inst Electr Electron Mater Eng* 2023;36:214–25.
- [10] Singh M, Truong K, Jandl S, Fournier P. Multiferroic double perovskites: opportunities, issues, and challenges. *J Appl Phys* 2010;107:09D917.
- [11] Yu H-L, Kang W-S, Lee J-H, Zate TT, Lee Y-J, Koo B-K, et al. Transparent high-performance piezoceramics through pressureless sintering. *J Adv Ceram* 2024;13:561–7.
- [12] Vopson MM. Fundamentals of multiferroic materials and their possible applications. *Crit Rev Solid State Mater Sci* 2015;40:223–50.
- [13] Le PG, Tran TL, Kim H-P, Jo W, Lee J-S, Fisher JG. Growth of single crystals of  $0.75(\text{Na}_{0.5}\text{Bi}_{0.5})\text{TiO}_3\text{-}0.25(\text{Sr}_{0.7}\text{Ca}_{0.3})\text{TiO}_3$  and characterisation of their electrical properties. *Open Ceram* 2021;6:100099.
- [14] Li C, Xu B, Lin D, Zhang S, Bellaiche L, Shrot TR, et al. Atomic-scale origin of ultrahigh piezoelectricity in samarium-doped PMN-PT ceramics. *Phys Rev B* 2020;101:140102.
- [15] Grinberg I, Rappe A. First principles calculations, crystal chemistry and properties of ferroelectric perovskites. *Phase Transitions* 2007;80:351–68.
- [16] Bersuker IB, Polinger V. Perovskite crystals: unique pseudo-jahn-teller origin of ferroelectricity, multiferroicity, permittivity, flexoelectricity, and polar nanoregions. *Condens Matter* 2020;5:68.
- [17] Pizzoli S, Ederer C. First principles studies of multiferroic materials. *J Phys Condens Matter* 2009;21:303201.
- [18] Shi J, Liu X, Zhu F, Tian W, Xia Y, Li T, et al. Oxygen vacancy migration and its lattice structural origin in A-site non-stoichiometric bismuth sodium titanate perovskites. *J Materiomics* 2022;8:719–29.
- [19] Bochenek D, Grabowski F, Niemiec P. Influence of cobalt admixture on the microstructure and dielectric properties of PFN ceramics. *Arch Metall Mater* 2011;56:1071–6.
- [20] Wook J, Jeong-Woo S, Jae-Hyeon C. Fabrication of bulk  $\text{PbTiO}_3$  ceramics with a high c/a ratio by Ni doping. *J Korean Inst Electr Electron Mater Eng* 2022;35:407–11.
- [21] Acosta M, Liu N, Deluca M, Heidt S, Ringl I, Dietz C, et al. Tailoring ergodicity through selective A-site doping in the  $\text{Bi}_{1/2}\text{Na}_{1/2}\text{TiO}_3\text{-Bi}_{1/2}\text{K}_{1/2}\text{TiO}_3$  system. *J Appl Phys* 2015;117:134106.
- [22] Scott JF. Room-temperature multiferroic magnetoelectrics. *NPG Asia Mater* 2013;5:e72.
- [23] Park JH, Lee JH, Cho JH, Jang JM, Jo W. Investigation on ferroelectric and magnetic properties of  $\text{Pb}(\text{Fe}_{1/2}\text{Nb}_{1/2})_3$  Fe-site engineered with antisymmetric exchange interaction. *J Korean Inst Electr Electron Mater Eng* 2022;35:

- 297–302.
- [24] Van Dover RB, Schneemeyer LF. The codeposited composition spread approach to high-throughput discovery/exploration of inorganic materials. *Macromol Rapid Commun* 2004;25:150–7.
- [25] Cho J-H, Lee J-H, Park J-H, Jang H, Yu H-L, Jang J, et al. Multiferroic properties in Fe-site engineered  $\text{PbFe}_{1/2}\text{Nb}_{1/2}\text{O}_3$  with distinct antisymmetric spin interaction. *Appl Phys Lett* 2023;122:112906.
- [26] Kresse G, Furthmüller J. Efficient iterative schemes for ab initio total-energy calculations using a plane-wave basis set. *Phys Rev B* 1996;54:11169.
- [27] Blöchl PE. Projector augmented-wave method. *Phys Rev B* 1994;50:17953.
- [28] Perdew JP, Burke K, Ernzerhof M. Generalized gradient approximation made simple. *Phys Rev Lett* 1996;77:3865.
- [29] Van De Walle A, Asta M, Ceder G. The alloy theoretic automated toolkit: a user guide. *Calphad* 2002;26:539–53.
- [30] Yamashita T, Hayes P. Analysis of XPS spectra of  $\text{Fe}^{2+}$  and  $\text{Fe}^{3+}$  ions in oxide materials. *Appl Surf Sci* 2008;254:2441–9.
- [31] Kozakov A, Kochur A, Googlev K, Nikolsky A, Raevski I, Smotrakov V, et al. X-ray photoelectron study of the valence state of iron in iron-containing single-crystal ( $\text{BiFeO}_3$ ,  $\text{PbFe}_{1/2}\text{Nb}_{1/2}\text{O}_3$ ), and ceramic ( $\text{BaFe}_{1/2}\text{Nb}_{1/2}\text{O}_3$ ) multiferroics. *J Electron Spectrosc Relat Phenom* 2011;184:16–23.
- [32] Marco JF, Gancedo JR, Gracia M, Gautier JL, Ríos El, Palmer HM, et al. Cation distribution and magnetic structure of the ferrimagnetic spinel  $\text{NiCo}_2\text{O}_4$ . *J Mater Chem* 2001;11:3087–93.
- [33] Fraygola B, Mesquita A, Coelho AA, García D, Mastelaro VR, Eiras JA. Fe valence fluctuations and magnetoelastic coupling in Pb-based multiferroics perovskites. *Phys Status Solidi* 2013;210:386–90.
- [34] Grosvenor AP, Biesinger MC, Smart RSC, McIntyre NS. New interpretations of XPS spectra of nickel metal and oxides. *Surf Sci* 2006;600:1771–9.
- [35] Mansour A. Characterization of NiO by XPS. *Surf Sci Spectra* 1994;3:231–8.
- [36] Biesinger MC, Payne BP, Grosvenor AP, Lau LW, Gerson AR, Smart RSC. Resolving surface chemical states in XPS analysis of first row transition metals, oxides and hydroxides: Cr, Mn, Fe, Co and Ni. *Appl Surf Sci* 2011;257:2717–30.
- [37] Kim HW, Ko H, Chung Y-C, Cho SB. Heterostructural phase diagram of  $\text{Ga}_2\text{O}_3$ -based solid solution with  $\text{Al}_2\text{O}_3$ . *J Eur Ceram Soc* 2021;41:611–6.
- [38] Goldschmidt V, Barth T, Lunde G, Zachariassen W. *Skr. norske vidensk. Akad. Mat.-naturv.*, vol. 8. Kl; 1926.



**Ahrom Ryu** is currently pursuing a combined M.S./Ph.D. in Materials Science and Engineering at Korea University in the Republic of Korea. Her research interests encompass the properties of sputtering thin films, as well as two-dimensional ceramic nanomaterials and their applications



**Ji-Hun Park** is currently a combined M.S./Ph.D. candidate under the supervision of Dr. Wook Jo in Materials Science and Engineering, Ulsan National Institute of Science and Technology (UNIST), Republic of Korea. He received his Bachelor of Materials Science and Engineering from UNIST in 2020. His research interests include searching the single-phase magnetoelectric coupled multiferroics at room temperature and its application.



**Wook Jo** is a professor at the Ulsan National Institute of Science and Technology (UNIST). His research interests include lead-free piezoceramics, dielectric materials, electrocaloric materials, room-temperature single-phase multiferroics, multiferroic photovoltaics, high power piezoelectric applications, large stroke actuator materials and in situ characterization of functional properties. His renowned work includes the perspective on lead-free piezoceramics and its applications. Wook Jo has published so far 100 peer-reviewed articles with about 21,000 citations.



**Ji-Won Choi** is a principal research scientist at KIST (Korea Institute of Science and Technology) and a professor in the Department of Nanoscience and Technology at UST (University of Science and Technology). He received a Ph.D. in Ceramic Engineering from Yonsei University. Following his Ph.D. studies, he served as a postdoctoral research associate at Cornell University. In 1994, he joined KIST as a research scientist. His research focuses on the development of dielectric thin films, transparent electrodes, all-solid-state thin film battery materials, and two-dimensional oxide nanosheets. He has authored over 200 peer-reviewed articles and holds more than 150 patents.